Distributed fibre optic sensing for sinkhole early warning: experimental study

Tobias Möller, Talia S. Da Silva Burke, Xiaomin Xu, Gianluigi Della Ragione, Emilio Bilotta, Christelle N Abadie

Möller, T. *et al*. *Géotechnique* [https://doi.org/10.1680/jgeot.21.00154]

Distributed fibre optic sensing for sinkhole early warning: experimental study

TOBIAS MÖLLER*, TALIA S. DA SILVA BURKE†, XIAOMIN XU‡, GIANLUIGI DELLA RAGIONE§, EMILIO BILOTTA‖ and CHRISTELLE N. ABADIE¶

This paper presents experimental work aimed at proving the feasibility of using distributed fibre optic sensing (DFOS) as an early warning system for sinkhole detection. The 1***g*** experiments were conducted using a plane-strain trapdoor and scaled to provide insight into the formation of a sinkhole in sand, in which DFOS cables were laid at selected depths. The DFOS data are compared with the geomechanics of the soil displacement, recorded using particle image velocimetry (PIV). It was demonstrated that the DFOS exhibits a signature strain profile at the location of the sinkhole, allowing a sinkhole to be located using the DFOS data. Differences in the PIV and DFOS data are, however, apparent – notably the strain magnitudes. Nonetheless, it is possible to estimate the size and location of the sinkhole at depth using the DFOS data. Using a preliminary study of the development of the zone of subsidence, for a range of relative densities, it is then possible to predict the extent of the damage zone at the ground surface. Such results show the potential for the incorporation of DFOS in the construction of critical infrastructure to enable early detection of sinkhole formation and thus provide an opportunity for remedial action to prevent catastrophic failures.

KEYWORDS: ground movements; model tests; monitoring

INTRODUCTION

Sinkhole failures are among the most common and disruptive shallow geohazards (Cooper & Calow, 1997; Banks *et al*., 2015). A sinkhole is a depression formed at the ground surface caused by the dissolution of carbonate rocks at depth, with progressive collapse of the ground towards the surface layer. Karstic terrains are particularly susceptible to sinkhole formation because of their composition of soluble rocks such as limestone, dolomites and evaporites (e.g. gypsum or chalk). The collapse of underground infrastructure, such as old mine shafts, can also cause the formation of sinkholes.

The development of linear infrastructure, such as roads, railways and bridges, is highly susceptible to sinkhole subsidence damage (Guerrero *et al*., 2008; Cooper, 2020). Despite an increasing interest in the threat posed by sinkholes (e.g. Sartain *et al*., 2011; Land *et al*., 2018; Land, 2019), there is no robust method available to date for predicting and locating sinkholes prior to ground surface collapse. Monitoring systems that provide a continuous record of potential indicators of the sinkhole formation – for example, surface deformations – are recommended (Gutierrez *et al*., 2008). Sinkholes can develop over extended periods, with measurable ground deformation developing over the course of several days, weeks or even years before the eventual collapse (Chang & Hanssen, 2014). This gives credence to the development of an early warning and detection system for sinkholes, which would protect infrastructure and save lives.

A number of existing monitoring techniques could be used to monitor sinkholes, primarily through measuring the progressive surface and subsurface soil settlement. These are summarised and compared in Table 1. These include geophysical surveys such as seismic wave propagation and ground penetrating radar (Guan *et al*., 2013), which are highly manual and have low area coverage and resolution. Satellite-based monitoring (interferometric synthetic aperture radar (InSAR)) (Chang & Hanssen, 2014) is able to cover extremely large areas but relies on the satellite's repeat-orbit cycle for its temporal frequency, commonly 4–6 days. Additionally, the low resolution of satellite imagery is not ideal for the identification of localised depressions. Distributed fibre optic sensing (DFOS) technologies (e.g. Brillouin optical time domain reflectometry (BOTDR)) (Guan *et al*., 2013; Inaudi, 2017) are well suited to identify sinkholes where the potential location is unknown, especially for monitoring long linear infrastructure, such as roads or railways, as they can be laid in continuous lines. An additional advantage is that they can provide subsurface deformation measurements, which would allow the identification of a sinkhole before its effects are evident at the soil surface. However, they rely on sufficient coupling at the interface between the fibre and the soil, as well as an understanding of the logged strain profile at depth. Monitoring settlements and ground deformation using fibre optic cables is a recent technique (Guan *et al*., 2013, 2015; Klar *et al*., 2014; Zhang *et al*., 2016; Inaudi, 2017) that still requires further understanding and experience of soil–fibre interaction and its effect on the obtained data.

The incorporation of fibre optic cables into earthworks could provide significantly improved information on the location, mechanisms and magnitude of subsurface ground

Manuscript received 10 June 2021; revised manuscript accepted 24 November 2021.
Discussion on this paper is welcomed by the editor.
* Department of Engineering, University of Cambridge, Cambridge, UK.
† Department of Civil Engineering, University of Pretoria, Pretoria, South Africa (Orcid:0000-0001-9393-8601).
‡ Cambridge Centre for Smart Infrastructure and Construction (CSIC), Department of Engineering, University of Cambridge, Cambridge, UK.
§ Department of Civil Engineering, University of Naples, Naples, Italy.
‖ Department of Civil Engineering, University of Naples, Naples, Italy (Orcid:0000-0002-3185-2738).
¶ Department of Engineering, University of Cambridge, Cambridge, UK (Orcid:0000-0002-5586-6560).

Table 1. Summary of different sinkhole detection techniques (Guan *et al.*, 2013; Chang & Hanssen, 2014)

Technique	Temporal frequency	Area coverage	Resolution	Advantages	Disadvantages
Monitor water or air pressure changes	High	Very low	n/a	Can monitor a location for long time spans.	Can only be used in small, localised areas.
Seismic wave propagation	Very low	Low	Low	Can accurately size and locate a sinkhole.	Requires an operative.
Ground penetrating radar (GPR)	Very low	Low	Low	Can accurately size and locate a sinkhole.	Requires an operative.
Interferometric synthetic aperture radar (InSAR)	Low	Very high	Medium	Can accurately determine ground deformations over large surface areas.	Temporal frequency depends on the satellite passing frequency.
Distributed fibre optic strain sensing (DFOS)	Very high	Medium	Very high	Can measure ground deformations along long continuous lines.	Converting strain profile into displacement profile is challenging.

movements in real time for newly built critical infrastructure over regions with high sinkhole susceptibility. However, this requires careful understanding and interpretation of the strain profile obtained in relation to the ground deformation and collapse mechanisms, to enable the retrieval of the potential sinkhole location with high precision. This paper presents a pilot experimental study, aimed at: (*a*) exploring the feasibility of using fibre optic cables to monitor subsurface ground movements in cohesionless soils where there is a progressive void formation at depth; (*b*) identifying the expected signature strain profile that such a monitoring system would exhibit if a sinkhole were to form; and (*c*) using the strain profile to locate and characterise the sinkhole. By addressing these three objectives, this paper proves the feasibility of quantifying the DFOS data in order to determine not only the location of a sinkhole but also predict its size.

Accordingly, the aim of the work presented in this paper is to analyse the recorded data collected from DFOS during the formation of a sinkhole in a controlled set of experiments at 1***g***. This is achieved through comparing the DFOS strain profile with the geomechanics of sinkhole formation in a cohesionless soil observed in controlled conditions with particle image velocimetry (PIV).

EXPERIMENTAL METHODOLOGY

Plane-strain trapdoor rig

A plane-strain trapdoor model, previously used for centrifuge modelling of arching in granular soils by da Silva Burke & Elshafie (2021), was used to simulate the subsurface formation of a void below a uniform soil layer. Tests were performed at 1***g***. This testing regime was chosen for the present study because it provides an efficient and simple method for running repeatable and consistent tests, notably to provide a proof of concept of the behaviour. Furthermore, the monitoring of distributed fibre optic strains at small scale with the analyser selected (discussed in more detail below) was not currently possible in the geotechnical centrifuge (Eichhorn, 2021). This set-up enabled an initial exploration of the use of fibre optic cables to monitor ground deformations and subsidence.

The rig is shown in Fig. 1, and consisted of a two-dimensional (2D) plane-strain box, with a poly(methyl methacrylate) (PMMA) window that can simulate the formation of sinkholes by lowering a trapdoor, actuated by way of a hydraulic cylinder (Fig. 1). The displacement of the trapdoor was recorded using linear variable differential transformers (LVDTs), mounted below the trapdoor. Experiments were terminated once a trapdoor displacement approaching 20 mm was achieved due to the limit on the piston stroke. The box has internal dimensions of 790 × 200 × 560 mm and the trapdoor has a width of 100 mm. The available soil height is approximately 370 mm, with a soil height of 200 mm being used in this paper. The PMMA window was polished, and the internal walls of the box were plated with polished hard chrome to minimise friction.

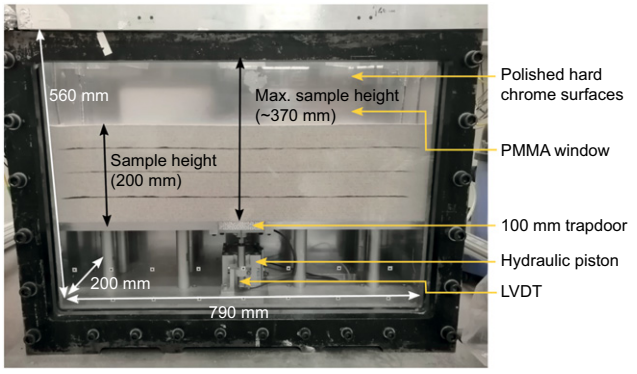

Fig. 1. The plane-strain trapdoor box

Test programme

In addition to proving the feasibility of using DFOS for monitoring of sinkhole formation, the test programme presented in this paper was also used to validate the testing procedures at 1***g*** and study the effect of relative density (D_R) on sinkhole propagation. Nine tests were performed in total and those used in this paper are described in Table 2, together with the aims of each test.

Data acquisition and monitoring

The transparent window of the plane-strain trapdoor box allows PIV to be used to measure the soil displacements. Layers of black sand placed at the location of fibre optic cables provided a clear visualisation of the soil deformation (Fig. 1). Images were taken using a pair of Canon Powershot G10 cameras. Initially, control markers were used to calibrate the cameras. Owing to unwanted data losses, later tests were performed using a ChAruCo board for calibration, removing the requirement for calibration markers (Eichhorn *et al.*, 2020). The recorded data were processed using the geoPIV-RG version of the PIV software described by Stanier *et al.* (2015). Further detailed description of this set-up can be found in Möller (2020) and Della Ragione (2020).

Fibre optic cables were placed at 50 mm intervals throughout the height of the soil to analyse and compare the strain profiles with the PIV (Fig. 2). The cable's diameter

Table 2. Testing programme

Test	D_R: %	I_R at trapdoor level	Laying technique	Testing objectives		
				Validate testing repeatability	Effect of D_R	Sinkhole characterisation
DR-18	18	0·62	Pinned	X		
DR-19	19	0·71	Pinned	X	X	X
DR-23	23	1·07	Pinned	X		
DR-40	40	2·58	Pinned		X	X
DR-52	52	3·64	Pinned and coated in sand	X	X	X
DR-54	54	3·82	Pinned	X		
DR-88	88	6·77	Pinned		X	X

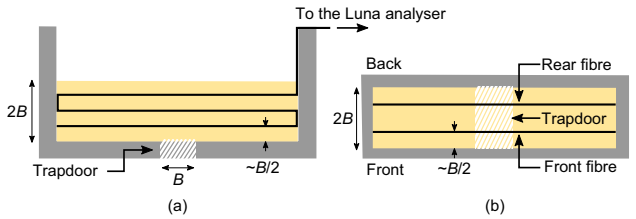

Fig. 2. An (a) elevation and (b) plan view of the trapdoor fibre layout

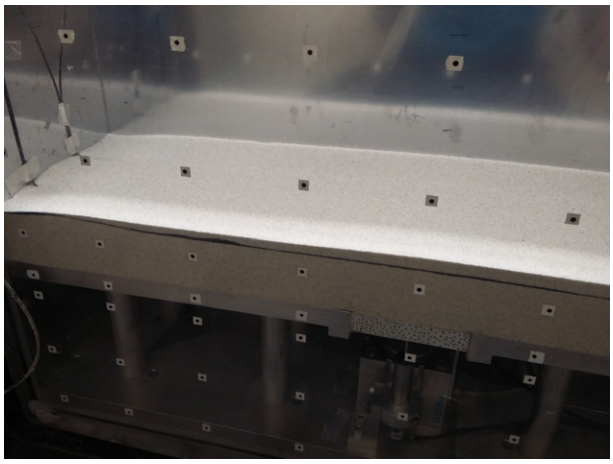

Fig. 3. An image showing the cables pinned to the edge of the box using tape

was 2 mm, with a 9 μm silica glass core. The Young's modulus of the fibre optic cable was 200 MPa. For each cable layer, the cables were pinned at both edges of the box to replicate the effect of overburden pressure in an infinitely long cable; excess slack between the two ends was removed before the cable was fixed in position. The cable was pinned by taping both ends to the box (Fig. 3). The DFOS results presented in this paper are focused on the sinkhole zone only, as the strain value did not always decay to zero – as expected for an infinitely long cable – within the confines of the box, in particular for low relative densities (DR-19). To enable this, a much longer box would be needed, and this would require a more complex experimental set-up and larger facilities (e.g. a sand pourer). However, the benefit of such a study is limited because the zone of interest for the signature strain profile is centred on the sinkhole. In the following, the results focus on a region of 600 mm centred on the trapdoor and provide a good compromise between relevance to the field and physical modelling feasibility.

In one of the tests presented, one of the fibres was coated in sand before laying (see Table 2), as part of a more extensive study investigating best DFOS laying practice and soil–cable interaction at 1g. For conciseness, the results of this study are not displayed here, but the data show that coating the fibre in sand increases the magnitude of the strain profiles (30% larger at the peaks for a trapdoor displacement of 2 mm) but does not alter the strain profile or its fundamental behaviour (i.e. location of peaks and approximate magnitudes of strains). As the main aim of this paper is the identification of trends in the DFOS strain and a signature profile above a developing sinkhole, this does not have a significant impact on the reported results.

The fibre optic cables were connected to a Luna ODiSI 6100 DFOS analyser, which enables measurement of the Rayleigh back-scattered light in optical fibres (Kechavarzi *et al.*, 2016). The spectral shift output from the analyser is linearly related to the strain and can be converted into strain data by multiplying the spectral shift by the calibration coefficient of the cable. This analyser has a particularly small gauge spacing (2·6 mm was used throughout this project), making it suitable for laboratory tests of the scale undertaken in this paper and promising significant scope for future work. The maximum measurement length for a gauge spacing of 2·6 mm is 10 m for a sampling frequency of 25 Hz; the analyser is capable of measuring strain over a range of ±12 000 με with an error of ±30 με (Luna, 2020).

Sample properties

All the tests were performed using dry Hostun sand (HN31), which is a fine-grained silica sand, with the properties given in Table 3. Four of the samples were prepared using an automatic sand pourer, described by Zhao *et al.* (2006), in order to obtain consistent relative densities. Three tests (DR-18, DR-19 and DR-23; Table 2) involved very low relative densities, which could not be prepared using the sand pourer; these were poured manually by placing the sand slowly from a very low height.

Scaling laws

When performing tests at 1g, scaling of the stress level with relation to modelling at full scale, or comparison with centrifuge modelling, is needed. This can be achieved using the framework from Bolton (1986)

$$I_R = D_R(10 - \ln p') - 1 \quad (1)$$

where I_R is the dilatancy index, D_R is the relative density and p' is the initial mean stress level. At 1g, the relative density is the most convenient critical parameter that experimentalists can adjust to be as representative as possible of the full scale by matching the dilatancy index, meaning that tests at low relative density at 1g correspond to a higher relative density in the field.

Table 3. Hostun sand (HN31) properties (da Silva, 2017)

Property	Symbol	Units	Value
Coefficient of uniformity	C_u	—	1·43
Average particle size	d_{50}	mm	0·356
Minimum void ratio	e_{min}	—	0·555
Maximum void ratio	e_{max}	—	1·010
Specific gravity	G_s	—	2·65
Critical angle of friction	Φ_c	degrees	35

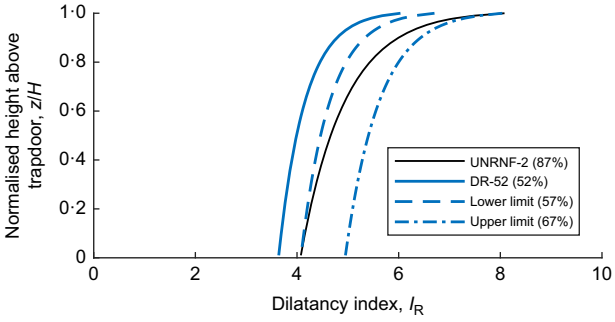

Fig. 4. Variation of dilatancy index (I_R) throughout the sample

This framework was applied for validation of the results through comparison of test DR-52 with test UNRNF-2 by da Silva (2017), which was performed in the centrifuge at 40g at a relative density of 87%. Both of these tests had the same H/B ratio – that is, 2. When comparing 1g with centrifuge models, it is only possible to match the relative dilatancies at a given depth in the sample, owing to the variation of dilatancy throughout the sample. For the work presented in this paper, it is appropriate to match the dilatancy index at the level of the trapdoor. To match the centrifuge test, $D_R = 57\%$ would be required at 1g. This means that throughout the remaining soil height, the 1g test will have a lower dilatancy, as demonstrated in Fig. 4, and hence will exhibit greater settlements. Unfortunately, it was difficult to obtain an exact relative density of $D_R = 57\%$ using the sand pourer. However, a relative density of $D_R = 52\%$ (test DR-52) was deemed close enough for comparison.

SINKHOLE FORMATION: PIV OBSERVATIONS

The first step in the data analysis was to determine the geomechanical behaviour of the soil. This was conducted by determining the soil settlement profiles as a function of height from the PIV results, and then using established models to fit these profiles. The fitted data were used to calculate the 'true' strain that would be experienced by a fibre optic cable if it matched the soil deformation perfectly. The mechanisms of deformation in the soil above the trapdoor were identified for models at various relative densities. A so-called 'damage zone' was identified and the behaviour of this zone at the soil surface was explored across relative densities. These results are discussed below.

PIV post-processing techniques

A Gaussian distribution can be used to model the soil settlements obtained during sinkhole formation (Costa *et al.*, 2009; da Silva, 2017). This technique has been extensively used in tunnelling (e.g. Mair, 2008; Marshall *et al.*, 2012). The use of two Gaussian distributions to fit the PIV data was explored in this paper: the standard Gaussian presented in equation (2) and the modified Gaussian as proposed by Vorster *et al.* (2005) and presented in equation (3), which allows an additional degree of freedom on the standard Gaussian distribution, resulting in the ability to model steeper slopes.

$$S_v = S_{max} \exp\left(\frac{-x^2}{2i^2}\right) \tag{2}$$

$$S_v = \frac{n}{(n-1) + \exp[\alpha(x/i)^2]} S_{max} \tag{3}$$

where S_v is the settlement at horizontal distance x from the trapdoor centreline; S_{max} is the maximum settlement (at the trapdoor centreline); i is the horizontal distance between the inflection point and the trapdoor centreline; α is a shape factor to alter the vertical location of the inflection point (thus steepening the distribution); and n is given by

$$n = e^{\alpha} \frac{2\alpha - 1}{2\alpha + 1} + 1 \tag{4}$$

Figure 5 compares the raw PIV data with both the standard and modified Gaussian distributions for various relative densities. This shows that for the bottom layer ($z = 50$ mm) the modified Gaussian provides the best fit, in particular as the trapdoor displacement increases. Both distributions work equally well for the other two layers. This aligns with the results from Vorster *et al.* (2005), suggesting that the steeper settlements experienced in sand can be better fitted using a modified Gaussian. As the distance above the trapdoor increases, the settlements become less steep and, hence, can be equally well modelled by a standard Gaussian. The modified Gaussian model is used in the remaining analysis.

During the formation of a sinkhole, the ground also experiences horizontal displacements. These were characterised as a function of the vertical settlement as shown in equation (5) (Klar *et al.*, 2014).

$$S_h = k \frac{x}{z} S_v \tag{5}$$

where S_h is the horizontal displacement; k is a factor; and z is the height above the trapdoor. Fig. 6 compares the raw PIV data to the least-squares regression fit from equation (5) for the horizontal displacements obtained in test DR-52 at $z = 50$ mm. The general trend indicates that this equation is well adapted to model the results. Similar results were noted in both the tests at lower and higher relative densities, giving confidence in the generic application of these observations.

For comparison with the DFOS data, it was necessary to extract strains from the PIV data, which are representative of those experienced by the fibres. The GeoPIV-RG software facilitates the extraction of horizontal and vertical strain fields. However, in order to extract strains representative of the DFOS data it was necessary to adopt a different technique, as the longitudinal strains experienced by the fibre are not equivalent to the horizontal or vertical strains extracted from the soil displacements measured by the PIV. This is due to the displaced shape of the fibre, which is unlikely to follow the soil movement exactly owing to (*a*) slippage at the soil–cable interface, and (*b*) pull-back tension applied to the cable by the overburden pressure, infinitely far away from the sinkhole (in the field, and in the case of the 1g experiment, by the pins). Accordingly, it was decided to convert the vertical settlement and horizontal displacement profiles into strain profiles to determine the equivalent strain that would be experienced by a cable that deformed exactly as the soil did. This was achieved by splitting the settlement profiles into distinct points and tracking the change in distance between neighbouring points; the fitted vertical settlement and horizontal displacement

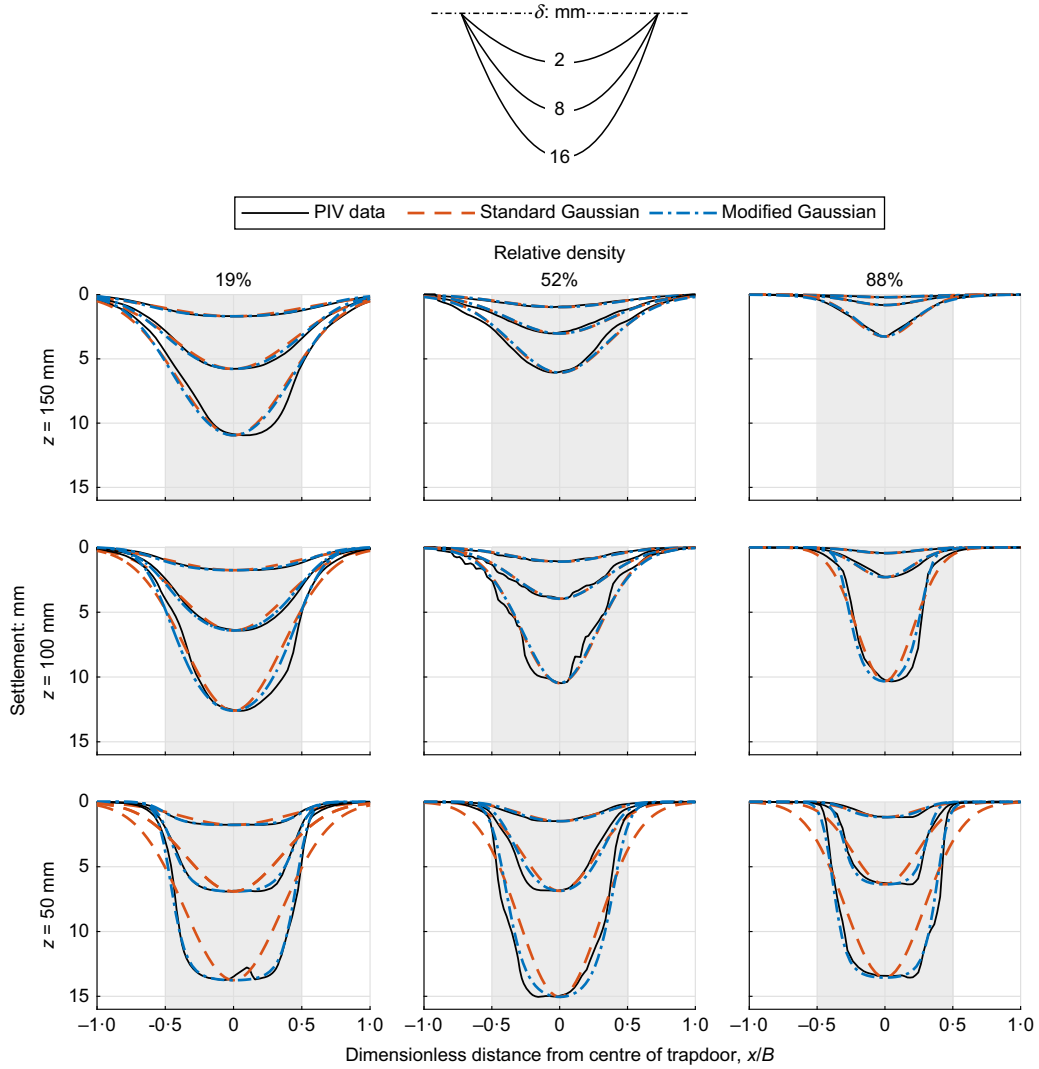

Fig. 5. Comparison of standard and modified Gaussian distributions to model soil settlement, at the heights of the three fibres, for three different relative densities, for $\delta = 2$, 8 and 16 mm

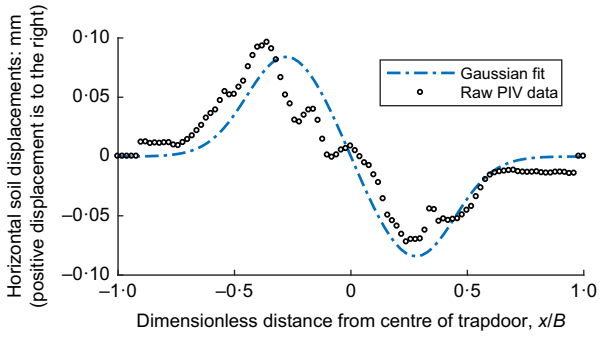

Fig. 6. Gaussian fit (equation (5)) of the PIV horizontal displacements for test DR-52 for $\delta = 2$ mm and $z = 50$ mm

profiles were used in this analysis, not the raw PIV data. This change in distance was then used to calculate a comparable strain and produce a combined strain profile by combining the two settlement profiles. This calculation process is explained in Fig. 7.

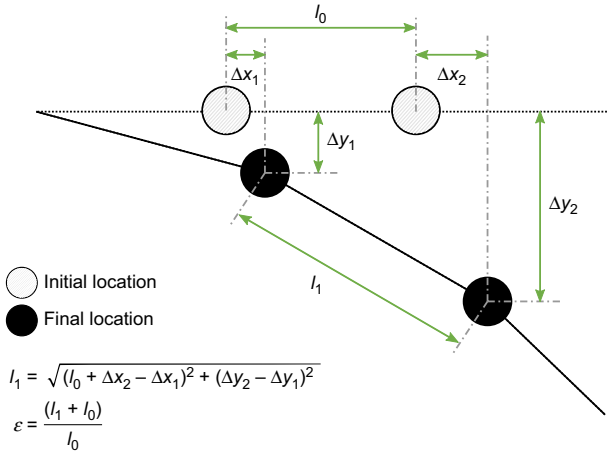

Fig. 7. Method for converting displacements into strain for PIV data using reference points with initial and final locations

Validation

The experimental set-up and data collection techniques were validated through comparison with (*a*) repeated tests and (*b*) data from published literature performed in the centrifuge to prove the repeatability and consistency of the testing procedures.

The PIV settlement profiles obtained in tests DR-54 and DR-52 – performed by two different researchers within the authors' team – were compared to validate the repeatability

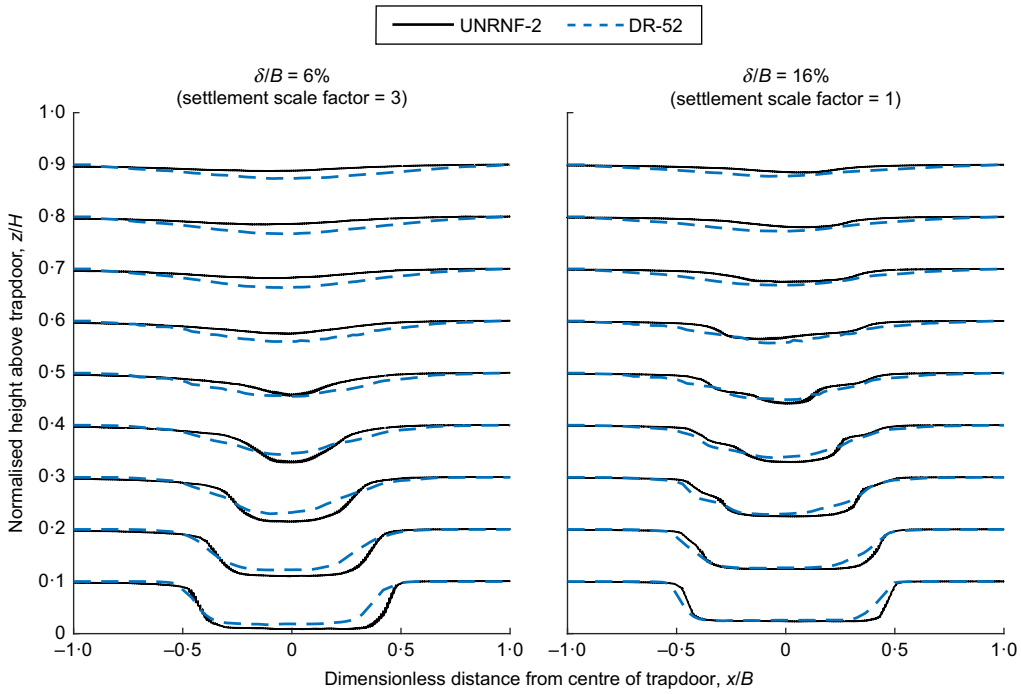

Fig. 8. Settlements obtained from PIV data, for two trapdoor displacements, for tests DR-52 and UNRNF-2 (da Silva, 2017)

of the testing procedures. A similar analysis was performed with tests DR-18, DR-19 and DR-23. For conciseness, the results are not displayed here, but they confirm that the profiles are very similar. These results are available in the online supplementary material.

Test DR-52 was also compared with a centrifuge test performed at 40***g*** by da Silva (2017) with the same H/B ratio (test ID: UNRNF-2); the results are presented in Fig. 8. As discussed in the section on scaling laws, test DR-52 had a lower dilatancy throughout the height of the model (see Fig. 4). This explains the discrepancies observed in the settlement profiles between tests UNRNF-2 and DR-52. The difference in dilatancy index is largest at the surface (Fig. 4) and this corroborates UNRNF-2 showing lower surface settlements when compared to DR-52 (Fig. 8). However, this comparison demonstrates that the settlement trough shapes are consistent between the two tests, suggesting that the soil mechanisms involved are similar. It also shows that the test results from the 1***g*** test campaign are conservative compared to what would be observed at higher, more representative, stress levels.

Definition of 'early' sinkhole formation and warning stages

To identify when the DFOS would be able to detect what corresponds to an 'early' stage of the sinkhole formation, theory from the mechanism of arching in granular soils was applied. Arching behaviour is usually classified into initial, transition and ultimate phases (Iglesia *et al.*, 2014; da Silva Burke & Elshafie, 2021), with the initial arching describing the rapid load decrease to a minimum value as the movement of the base increases. This transition point usually occurs at displacements between 1 and 2% of the trapdoor (i.e. void) width (Dewoolkar *et al.*, 2007). Based on this observation, any change in DFOS strain profile detected while the soil is in this initial phase of arching ($\delta \leq 2$ mm) is here classified as an 'early' detection.

The arching mechanism progresses with the successive formation of shear bands, and ultimate arching occurs with the formation of vertical shear bands from the trapdoor ('void') edges to the soil surface (Iglesia *et al*, 2014; Jacobsz, 2016; da Silva Burke & Elshafie, 2021). 'Medium warning' was defined as the period prior to the shear bands reaching the surface. This point can be found by locating the change in gradient of the surface settlement curve (Dewoolkar *et al.*, 2007) or by observing the drop in the angle of dilation – that is, the angle between the vertical and the tangent of the identified shear bands. For the results presented in this paper the 'medium warning' stage is defined as $2 \text{ mm} < \delta \leq 12{\cdot}5$ mm.

'Late warning' was hence defined as being post the formation of vertical shear bands ($\delta > 12{\cdot}5$ mm). Fig. 9 highlights these three different stages through the change in evolution of (*a*) the normalised surface settlements, (*b*) the surface settlements normalised by the trapdoor displacement and (*c*) the angle of dilation for three different relative densities. The figure additionally highlights three pertinent trapdoor displacements to represent the three stages: (*a*) $\delta =$ 2 mm has been chosen to represent the 'early' stage, as this is the most reliable data point found in the 'early' stage, (*b*) $\delta = 8$ mm and (*c*) $\delta = 16$ mm have been chosen to represent the 'medium' and the 'late' stage, respectively, as both are roughly in the middle of their stages. These three trapdoor displacements are used in the following analyses.

Influence of relative density

The PIV data were used to plot the shear strains throughout the sample, for three different relative densities and the three warning stages (Fig. 10). The purpose of this was to establish whether the different densities resulted in different mechanisms of behaviour in the propagation from the sinkhole to the soil surface, thus requiring different approaches to be adopted in the use of fibre optic strain data to determine the sinkhole size and location. As expected, shear bands emanate from the edges of the trapdoor and gradually propagate to the surface. However, the behaviour varies significantly with relative density. For the medium dense and the dense samples, initial shear bands form a triangular wedge. Eventually, a second set of parabolic shear bands forms, reaching further up the sample. This aligns with the results commonly found in the literature (Dewoolkar

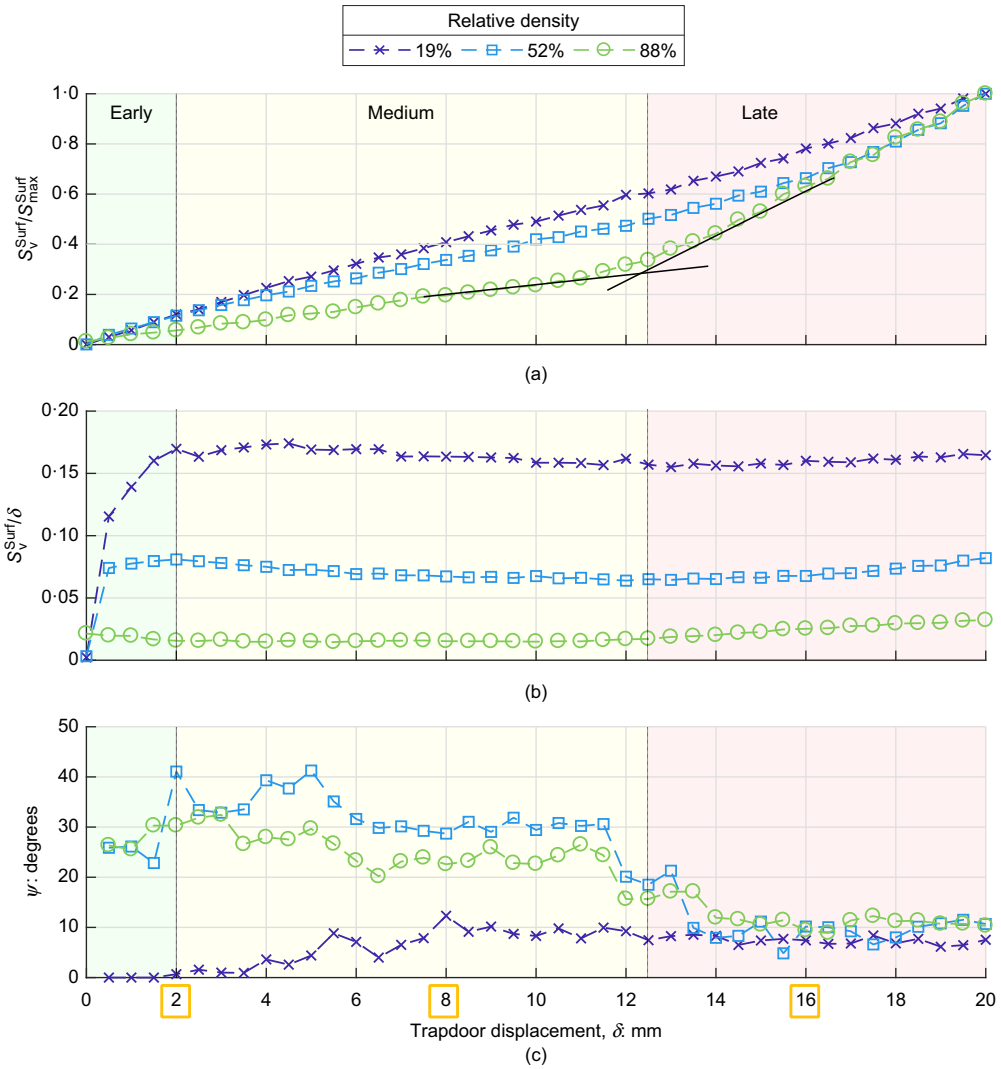

Fig. 9. Defining 'early', 'medium' and 'late warning' based on (a) the normalised surface settlements; (b) the surface settlements as a ratio of the trapdoor displacement; and (c) the angle of dilation for three different relative densities

et al., 2007; Iglesia *et al.*, 2014; da Silva Burke & Elshafie, 2021). However, this does not occur in the loose sample. Instead, the initial shear bands are close to vertical, with later shear bands gradually tending inwards. This would suggest that, instead of the usual trend in shear band formation as the soil dilates, the soil is densifying, leading to an increase in the angle of dilation. This compares favourably with the results of Igwe *et al.* (2012).

To further explore this effect, the angles of dilation were extracted by taking the angle between the shear band at the trapdoor and the vertical axis (Costa *et al.*, 2009), reported in Fig. 9(c). The trends confirm that the test at low relative density behaves significantly differently to the other tests, with an initial value of the angle of dilation equal to zero, followed by an increase caused by densification. The medium dense and dense samples initially exhibit a gradual decrease in the angle of dilation until a sudden drop in dilation angle is reached when the parabolic, secondary shear bands are formed.

Further effects of relative density can be observed in the settlement profile characteristics. Fig. 11 explores the behaviour of the modified Gaussian inflection point (see equation (3)) with height, where it is observed that the location of the inflection point remains constant throughout the height of the sample. However, it is noteworthy that the greater the relative density, the closer the inflection points are to the origin. Fig. 11 also explores the behaviour of the trough width with height, where the trough width is defined as the point on the settlement profile where $dS_v/dx = 0{\cdot}1S_{max}/i$ (da Silva, 2017). Similarly, the trough width decreases as the relative density increases. However, unlike the inflection points, the trough width increases with height, indicating that the settlement profiles are widening as the height of the sample increases. This suggests that the deformation is propagating towards the surface in a funnel-like manner.

Damage zone

When monitoring sinkholes in the field, predicting the damage zone that the sinkhole can potentially cause at the ground surface is critical information. Accordingly, a damage zone extent, w_D, is defined as the width of the settlement trough over which the slope is greater than 1/500, which is an acceptable settlement threshold above which buildings are likely to suffer superficial damage (Rankin, 1988; Son & Cording, 2005).

The evolution of the normalised surface damage zone width, $\tilde{w}_D^{Surf} = w_D^{Surf}/B$, with increasing trapdoor displacement, $\tilde{\delta} = 100\delta/B$, is shown in Fig. 12(a), and fitted with the following evolution law

$$\tilde{w}_D^{Surf} = K_D\tilde{\delta}^a \tag{6}$$

K_D is a dimensionless coefficient, which decreases linearly as a function of D_R, as displayed in Fig. 12(b). The power

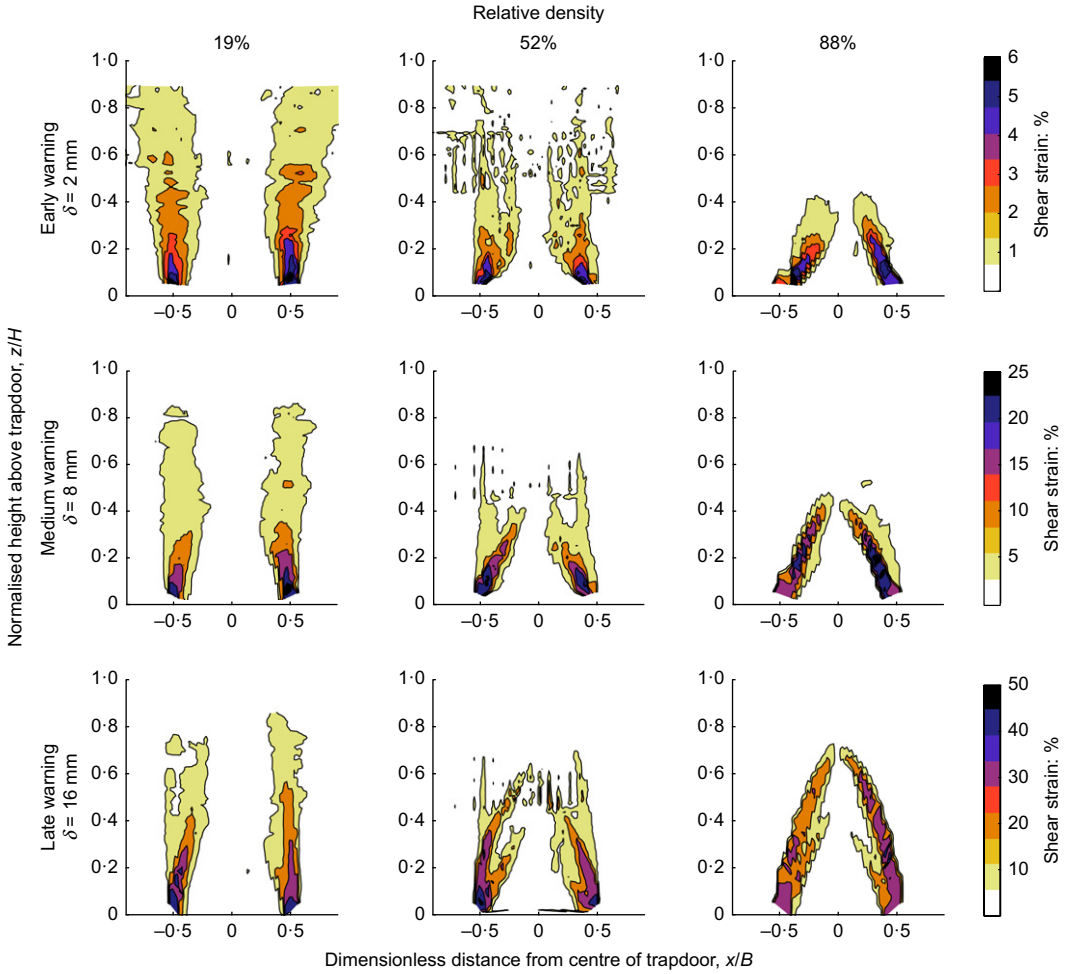

Fig. 10. Plots of shear strains throughout the sample taken from PIV data, for three different relative densities, for 'early', 'medium' and 'late warning'

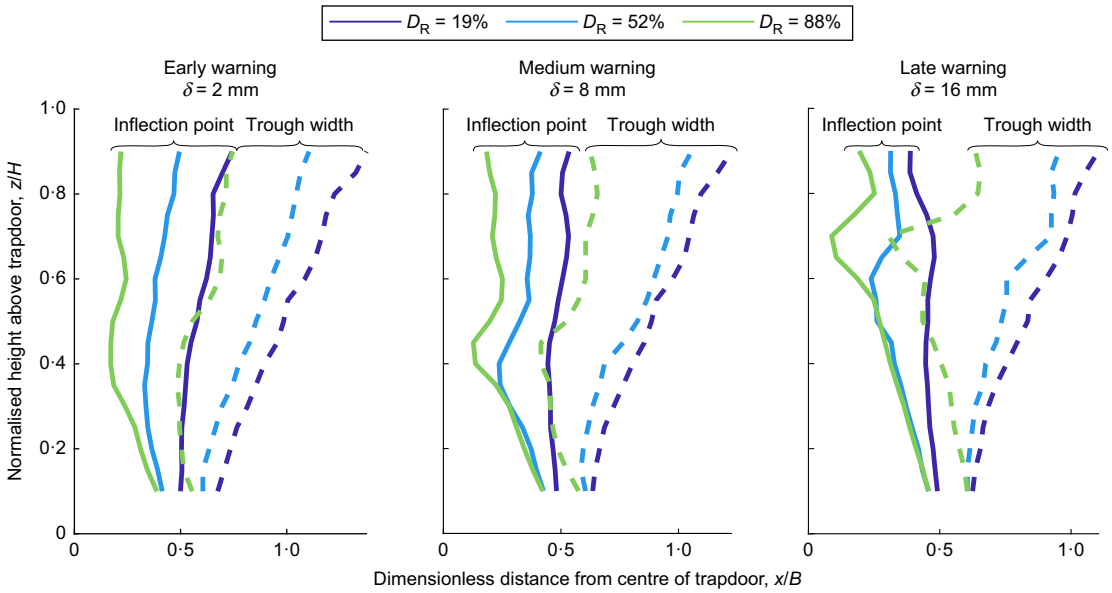

Fig. 11. Inflection point and trough width with height, across three relative densities and three trapdoor displacements

coefficient a is an exponentially increasing function of D_R, as shown in Fig. 12(c). The equation shows that for any given δ, the surface damage zone width decreases with relative density, but this decrease diminishes as δ increases. A log law can also be used with reasonable accuracy to model the data, but presents a less intuitive equation for interpretation of the results.

This study offers an indication of how a damage zone could be identified for specific geology and a given threshold of surface settlement, with the aim of outlining a method for

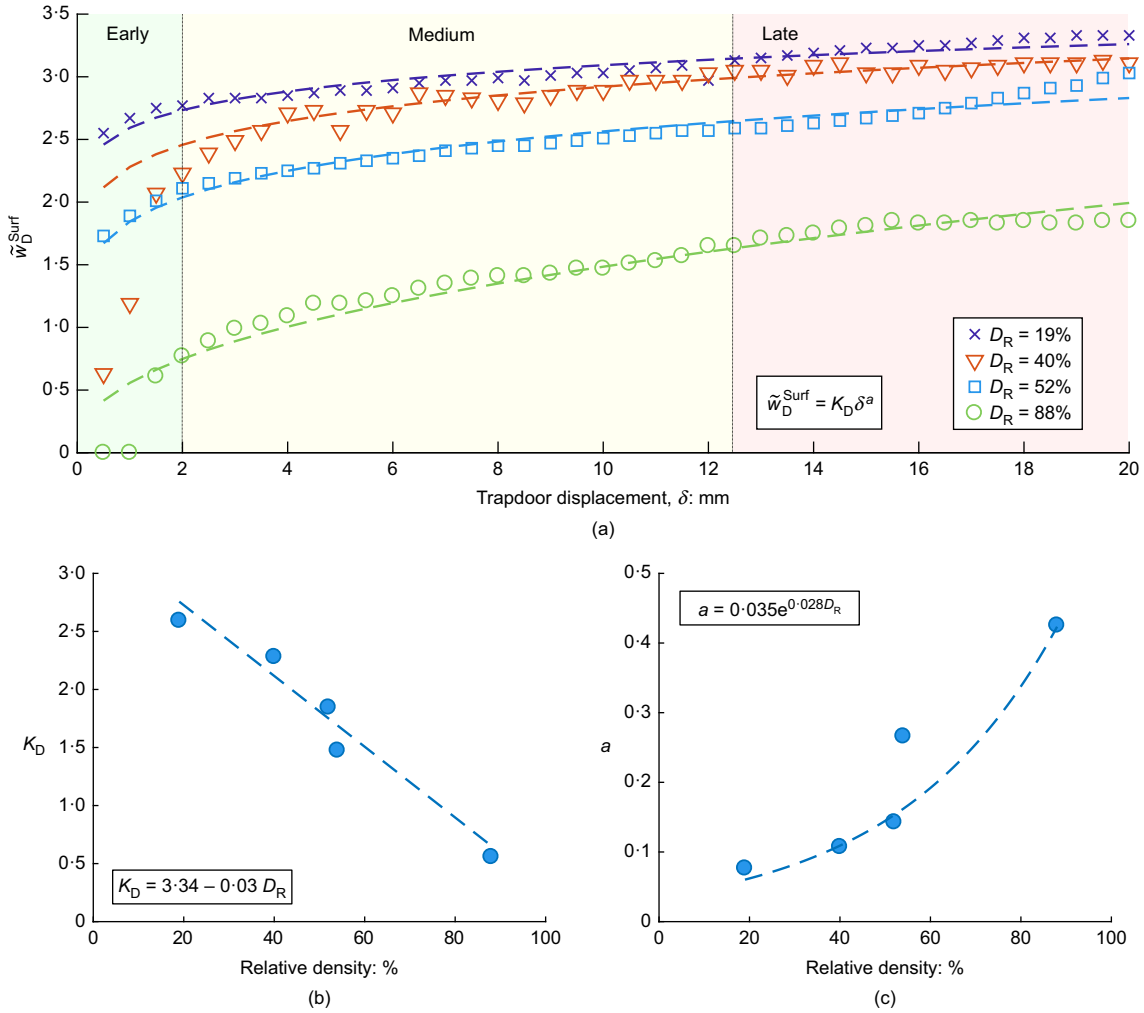

Fig. 12. (a) Comparison of the surface damage widths with the power law (equation (6)) for different relative densities; (b) linear fit to K_D; (c) exponential fit to a

the use of the DFOS data in the second part of the paper. However, the damage zone estimation relies on the sinkhole propagation mechanism, which varies significantly depending on the soil type and in situ stresses. In addition, the definition of the damage zone is specific to the type of infrastructure being built. The method would therefore need to be extended to match different types of terrain and infrastructure in future research but provides sufficient ground for the development of the DFOS data analysis targeted in this paper.

EARLY WARNING STRAIN PROFILE FROM DFOS

Capitalising on the characterisation of the soil deformation behaviour from the PIV data, the output from the DFOS is here processed to establish whether the fibre optic cables do exhibit a signature strain profile as the development of the 'sinkhole' – that is, the lowering of the trapdoor – progresses. The method used to identify such signature strain profiles is detailed below, together with guidelines on how this signal can be used to infer the location and potential size of the detected sinkhole.

DFOS post-processing techniques

The resultant fibre optic strain profiles, determined by multiplying the spectral shift output from the analyser by the calibration coefficient of the cable, display a double-peak profile with a central dip. The symmetrical nature of the strain profile can be used to determine its location in relation to the trapdoor. Examples of these results are shown in Fig. 13 for three different relative densities.

The results show that the fibre optic is successfully able to detect the early stage of the formation of a sinkhole, and at shallow buried cable depth (see $\delta = 2$ mm at $z = 150$ mm). At this early stage, the same general shape profile is exhibited at all three layers – that is, negative strain in the centre with positive strain further away from the trapdoor centre and tending to zero as the distance from the trapdoor increases. The greater the relative density, the faster the strain value tends to zero. This corresponds with the result observed in Fig. 11 where the width of the profile increases with decreasing relative density. This suggests that the greater overburden pressure in soil of higher relative density is effectively moving the cable pinning location towards the trapdoor, leading to a narrower field of influence, as expected. As mentioned earlier, for the low-density test (DR-19), the width of the box was not sufficient to monitor strains in the cable until a point of zero-strain was reached. The strain profile is wider higher up in the soil – that is, the positive peaks are further away from the centreline. This concurs with the widening settlement profile observed in Figs 5 and 11. As the trapdoor displacement increases, the fibre optic strain profile results in a positive strain on the centreline, indicative of the entire cable moving into tension. This phenomenon is more pronounced closer to the trapdoor.

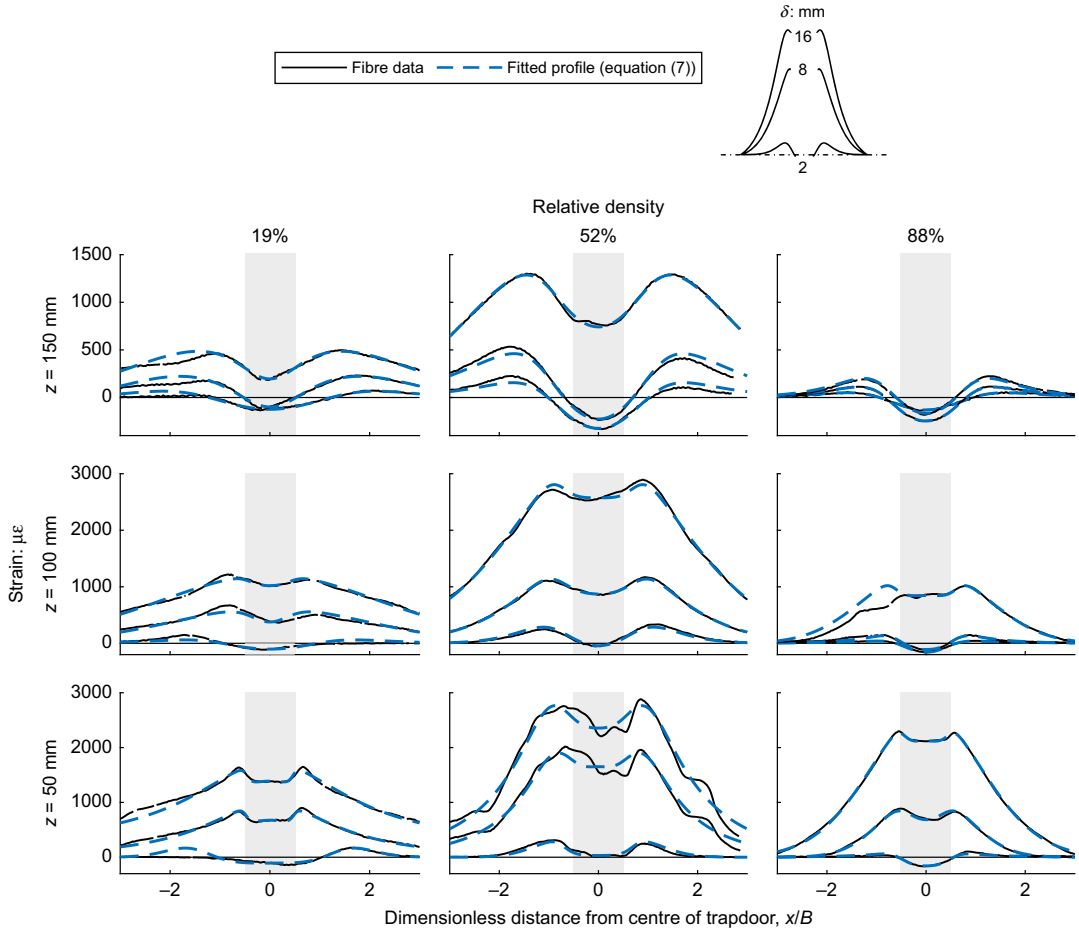

Fig. 13. Comparison of the fibre strain profile with the summation of Gaussian distributions (equation (7)), at the heights of the three fibres, for three different relative densities, for $\delta = 2$, 8 and 16 mm

To facilitate the processing of the fibre optic strain data, a function consisting of the summation of two modified Gaussian distributions was used to fit the data. This follows a similar procedure as for the processing of the PIV data and is here given by

$$\varepsilon = S_{\text{peak}} \frac{o}{(o-1) + \exp[\beta(x/j)^2]} - S_{\text{dip}} \frac{q}{(q-1) + \exp[\eta(x/r)^2]} \quad (7)$$

where ε is the fibre optic strain; S_{peak}, S_{dip}, β, η, j and r are fitting parameters determined from a least-squares regression to the DFOS data, with o and q defined from equation (8). S_{peak} and S_{dip} are strains representative of the peak strain in equation (7) and the drop in strain associated with the central dip, respectively. β and η are shape factors to alter the vertical locations of the inflection points (j and r) (thus steepening the distribution).

$$o = e^{\beta} \frac{2\beta - 1}{2\beta + 1} + 1 \text{ and } q = e^{\eta} \frac{2\eta - 1}{2\eta + 1} + 1 \quad (8)$$

Figure 13 compares the raw DFOS data with the function defined above and demonstrates that this equation provides a good fit to the Luna profile throughout the different relative densities, heights and trapdoor displacements.

Settlement behaviour

Figure 14 shows the DFOS strain at the centreline at the three selected layers as a function of the trapdoor displacement ($\delta \leq 3$ mm). This is compared to the surface settlement measured using PIV at the centre of the trapdoor. The graph shows that the fibre optic strain profile clearly detects subsurface ground deformations during the 'early' phase and prior to large surface deformation. The fibres are capable of identifying the formation of a sinkhole while surface settlements remain less than a millimetre. This demonstrates the potential for locating sinkholes using fibre optic cables before significant impact on the surface is identified. In addition, this highlights the advantage to be gained by the use of subsurface monitoring techniques in comparison to surface deformation monitoring.

Signature strain profile

The strain profiles from the fibre optic cables resulted in a distinct signature profile across tests and heights (see Fig. 13). A typical example is shown in Fig. 15(a) for test DR-52 at $z = 150$ mm. As identified previously, the strain profiles are characterised by a double peak and a trough, located at the centre of the sinkhole. In general, the initial strain in the centre is negative, but as the trapdoor displacement increases, this becomes positive as the fibre is under increasing tension caused by the competition between the static soil overburden pressure at the edges of the fibres versus the downwards soil movement towards the centre, which leads to the strain profile moving out of the negative zone.

Comparison to the vertical, horizontal and combined PIV strain profiles determined using the procedure explained in Fig. 7 is shown in Figs 15(b), 15(c) and 15(d) to explore the conformance between the soil and fibre optic cable

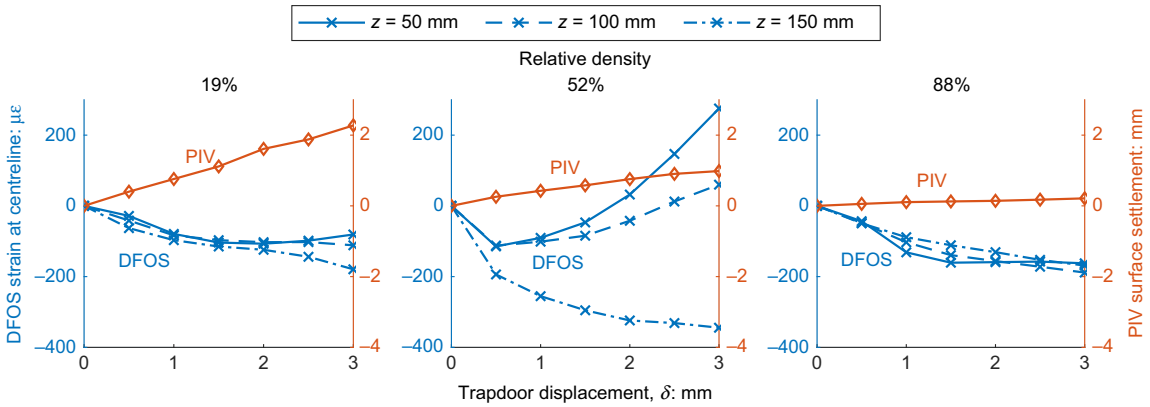

Fig. 14. DFOS strains at the centreline above the trapdoor at the three different layers, compared to the surface settlement (obtained from PIV), for different relative densities

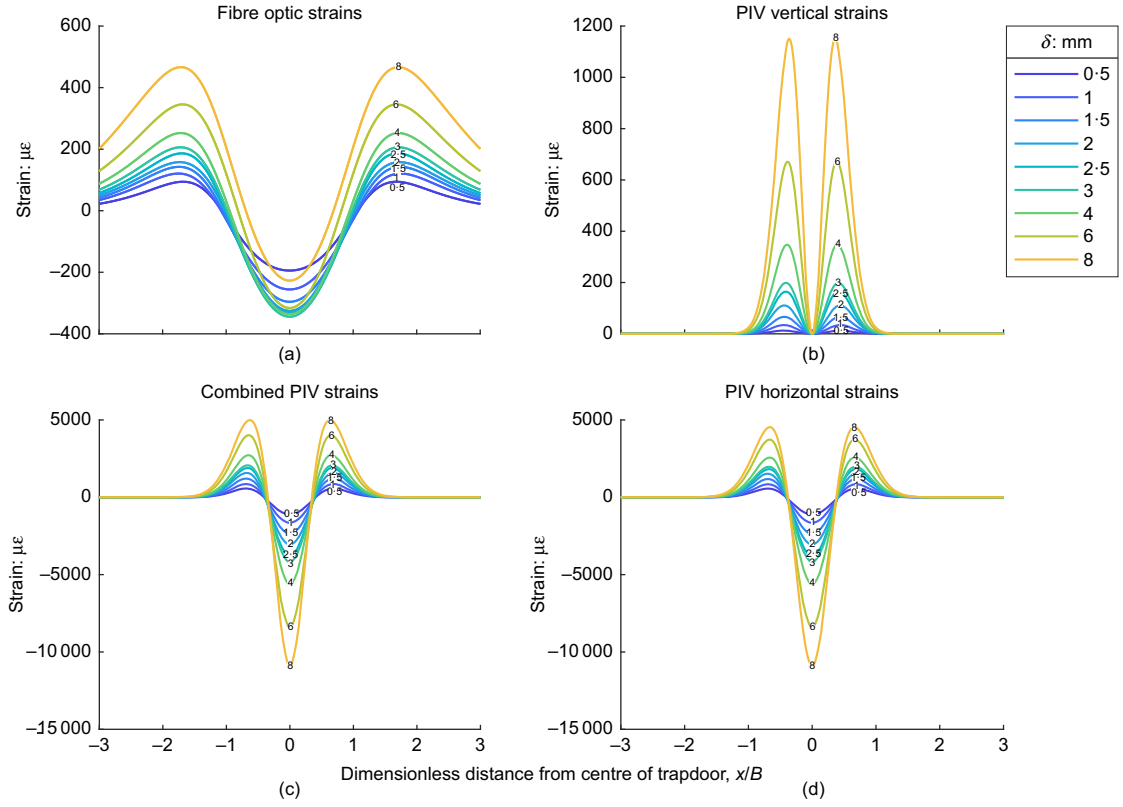

Fig. 15. (a) Fibre strain profile for the rear fibre; (b) vertical, (c) combined and (d) horizontal strain profiles obtained from the PIV data, all for z=150 mm, in test DR-52

deformations. The fibre optic cable has a very low stiffness perpendicularly to its longitudinal axis and hence can follow vertical movements easily. This is particularly important for this application, where most of the ground movement is expected to be vertical. However, the fibre has an axial stiffness of 200 MPa and hence longitudinal movements of the fibre generate strains as the fibre is stretched, distorting the original longitudinal strain profile, and by extension, the horizontal strain profile observed from PIV.

This is well demonstrated in Figs 15(b) and 15(d), where the vertical and horizontal strain profiles obtained from the PIV data are compared. Although both profiles have a double peak, they are also very different, with the vertical peaks located within the trapdoor extents whereas the horizontal peaks lie outside. The vertical strain profile does not exhibit any negative strains, whereas the horizontal profile does, and the magnitudes of the horizontal strains are larger than the vertical strains. This demonstrates that the horizontal strains dominate the combined PIV strain profile observed in Fig. 15(c), which indeed is very similar to the horizontal profile and includes negative regions that are only present in the horizontal profile. Accordingly, the fibre optic cable is measuring mostly the horizontal strains in the ground, with the differences explained by the cable axial stiffness and the (lack of) coupling between the cable and the soil.

When comparing the horizontal PIV with the fibre optic strain profiles, Figs 15(a) and 15(d), there are several important differences. First, the PIV strains are approximately one order of magnitude larger than the fibre optic strains. This is likely to be caused by the fibre not deforming exactly with the soil, and therefore relative movement between the fibre and the soil: this is potentially due to slippage along the fibre axis, as well as cutting of the fibre

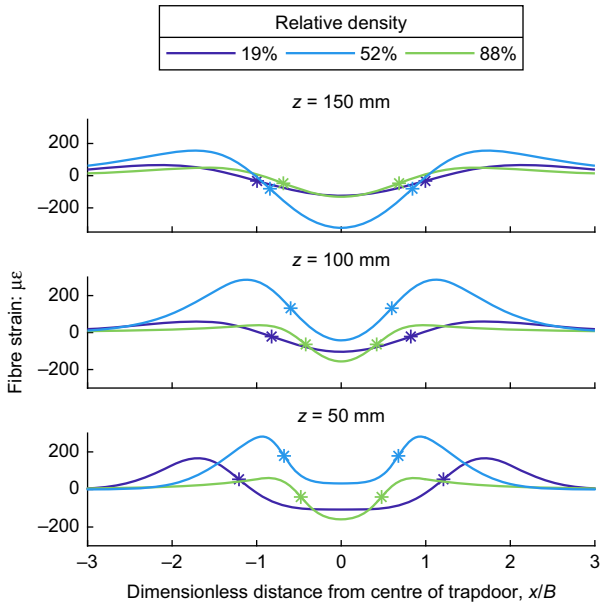

Fig. 16. DFOS trapdoor width estimates, for the three heights and δ = 2 mm, across three relative densities

into the soil perpendicular to the fibre. Second, the fibre optic strain profile is significantly wider than the PIV profile. Finally, the fibre strain profile does not stay vertically centred on the zero-strain axis as it does for the PIV. This is due to global tension in the cable – as the deformation increases significantly – caused by the fixity of the fibre at each end of the box. The tension in the fibre at the edges of the box has not yet decayed to zero and this prevents the DFOS strain profile from remaining vertically centred on the zero-strain axis. Caution must hence be exerted when interpreting solely the fibre optic strain profile to infer the soil mechanics beneath soil surface settlement.

Despite these limitations, the fibre optic strains exhibit a signature profile with a global minimum indicating the location of the centre of the trapdoor – that is, sinkhole – and provide a sufficiently large reading even at low trapdoor displacement levels. This thus shows great potential to be used in identifying the formation and location of sinkholes that develop below a monitoring cable.

Sinkhole size prediction

Finally, the fibre optic data can be used to estimate the size of the void that is forming. This depends on the distance of the cable above the developing void, and how the sinkhole deformation is propagated through the soil. The results at the transition of the early warning stage (i.e. $\delta = 2$ mm) are plotted in Fig. 16 for tests DR-19, DR-52 and DR-88, where the trapdoor size is highlighted in grey. It was found that the point of maximum gradient of the DFOS strain profile provided a reasonable correlation with the void size. The width of the trapdoor estimated from the DFOS strain profile was defined as w_e and this width is also highlighted in Fig. 16 using dashed lines.

To explore the accuracy of these predictions between different tests and at different heights above the trapdoor, an over-prediction coefficient, Ω_t, has been defined as

$$\Omega_t = \frac{w_e}{B} \tag{9}$$

where w_e is the trapdoor width estimate and B is the trapdoor width. If $\Omega_t > 1$, the DFOS data overpredict the sinkhole size. The results of Ω_t as a function of relative density for the 'early', 'medium' and 'late' stages are shown in Fig. 17(a). The graphs show that the majority of the trapdoor width predictions are overpredictions, especially as the distance between the fibre and the trapdoor increases. At the highest fibre location above the trapdoor ($z = 150$ mm), the DFOS strain profile shows a greater tendency to overpredict the sinkhole size, and this is more pronounced at lower relative densities. If the DFOS strain profile is interpreted as a function of the width of the subsidence zone created by the sinkhole, then these overpredictions concur with the results shown in Fig. 11 where the formation of a funnel-shaped zone of subsidence is shown, with wider funnels for samples of lower density. This trend is consistent as trapdoor displacement increases.

As a result, the size of the trapdoor can be predicted using the fibre strain profile alone, and consequently, provides confidence that DFOS can be used as a conservative early warning of not only sinkhole formation and location, but also the sinkhole size, and by extension, the surface damage zone, as detailed below. These observations are based on tests on a single soil type and using a single H/B ratio; as such the predictions are therefore intended to be indicative only, when related to scenarios outside those reported in these tests, but still considered useful to indicate expected behaviour and future research directions.

Application and future work

To conclude, the DFOS data were used to predict the surface 'damage zone' as described in the PIV section and compared with the data from PIV following the method below.

Step 1. Identify the signature strain profile, thereby locating the centre of the sinkhole.
Step 2. Estimate the size of the sinkhole by calculating the width between the points on the fibre strain profile with the maximum gradient.
Step 3. Assuming a known relative density (obtained through site investigation), use equation (6) to calculate $\hat{w}_D^{Surf}$ for the 'late' stage.
Step 4. Calculate the ultimate surface damage zone, w_D^{Surf} by multiplying the result of step 3 by the result of step 2.

The accuracy of these predictions is presented in Fig. 17(b), for which Ω_D has been defined as the predicted ultimate damage zone (DFOS) divided by the actual ultimate damage zone (PIV). The results show that almost all of the predictions overpredict the damage zone, in particular, if the fibre is embedded at shallow depth (i.e. $z = 150$ mm). This is valuable as it provides a conservative estimate of the zone where remedial (ground)work might be necessary should the sinkhole fully develop.

When applying this technique in the field, noise is expected to be present in the strain readings. Furthermore, the fibres likely to be used in the field are more robust than those used in the laboratory. However, it is reasonable to expect that the signature strain profile, growing in magnitude over time, could still be located in the data. A field test campaign is scheduled to further explore and validate this work.

Another consideration when comparing the laboratory test to the expected field behaviour is in the effective number of points that are able to be monitored across the width of the sinkhole. In the laboratory test, the high resolution of the optical frequency domain reflectometry (OFDR) analyser allowed approximately 38 points to be monitored across the trapdoor (i.e. sinkhole). In the field, Brillouin technology typically has a spatial resolution of 0·5 to 1 m.

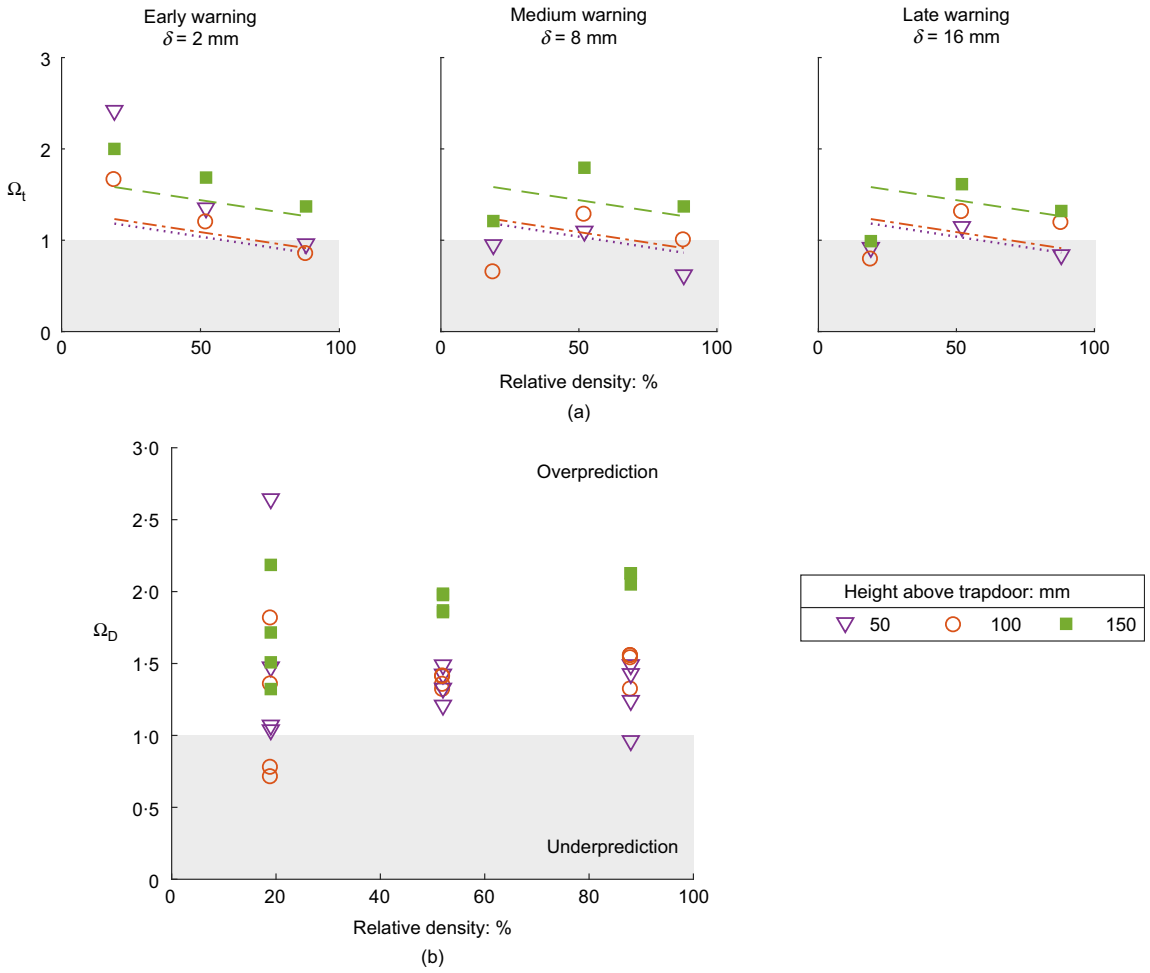

Fig. 17. (a) Ω_t data collected for $\delta = 2$, 8 and 16 mm; and (b) Ω_D data collected for $\delta = 2$, 4, 6 and 8 mm

For a sinkhole of 5 m dia., this would result in the monitoring of only five to ten points across the sinkhole. To explore this effect, the OFDR analyser data were averaged over several adjacent points and the strain profile for a reduced resolution was determined. The results for the averaging of two, four and seven adjacent readings (approximately 19, ten and five points across the trapdoor) are shown in Fig. 18 for the cable at $z = 150$ mm in test DR-88. The results show that even at reduced resolutions the data are able to identify the signature strain profile and would still provide valuable information.

Owing to experimental constraints for the use of the OFDR analyser, the proposed model could only be calibrated for low-stress states at 1g, and a particular trapdoor width and soil height. Accordingly, no attempt has been made to scale the data presented in this paper directly to sinkholes found in the field. Future work will aim at extending this study to relevant stress regimes and addressing the effects of soil saturation and relevant soil profiles.

A further limitation of the experimental work performed is the plane-strain nature of the box; this limits the ability to predict the fibre optic response when the cable is not located directly above the developing sinkhole. Further work will be required in order to explore the effects of sinkhole location relative to the fibre optic cables.

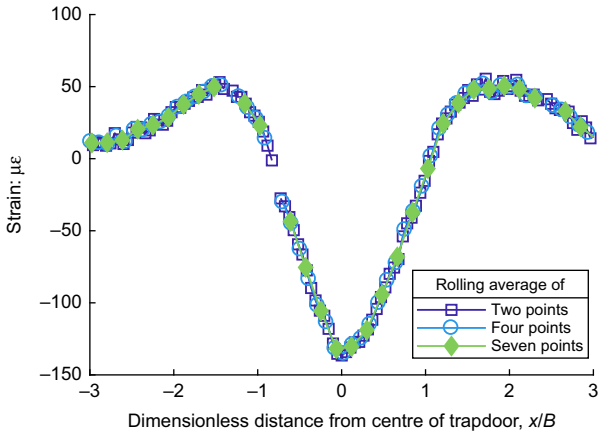

Fig. 18. DFOS strain profiles with varying resolutions for test DR-88 for z=150 mm and δ=2 mm

CONCLUSIONS

The 1g tests in cohesionless soils were performed with a 2D plane-strain trapdoor rig to explore the geomechanics of sinkhole formation and prove the feasibility of using DFOS as an early warning system. PIV was used to monitor the soil behaviour accurately, and these data were compared to the fibre optic data. The results show that the fibre optic data clearly exhibit a signature strain profile that is comparable to the horizontal strains recorded through the PIV data. Some differences from the PIV strain profile were, however, highlighted: first, the fibre optic cable strain profile is wider than the width of the soil settlements, due to the cable axial stiffness and the lack of coupling. Related to this, the

magnitude of the strain recorded from the DFOS is an order of magnitude lower than that measured from the PIV. It is worth noting, however, that the absolute magnitude of the fibre strain is not relevant when predicting a sinkhole, as it is the shape of the strain profile that is used to identify and quantify the sinkhole. In addition, if the DFOS cable is only able to detect strain changes at unacceptably large deformations where damage to the infrastructure would already have occurred, then it would not be suitable as an early warning system. This 'signature' strain profile with a double peak and local depression is expected to be uniquely related to ground disturbances resulting in local subsidence at a sufficiently early stage in the formation of the sinkhole.

As a result, the key outcome from this study is that the early formation of a sinkhole can be detected using the DFOS data: the sinkhole location can be identified using the centre of the signature strain profile, and the approximate width can be estimated using the distance between the points of maximum slope on the fitted double modified Gaussian distribution of the DFOS data. From this, the ultimate surface damage zone can then be predicted using the power law in equation (6).

If the proposed field test campaign is conclusive, the use of DFOS to signal sinkhole formation will become a viable solution for early warning of sinkhole formation. In light of this, the current work provides an initial proof of concept on the potential use of DFOS to remediate soil subsidence for newly built critical infrastructure for which laying fibre optic cables is appropriate.

ACKNOWLEDGEMENTS

The authors are grateful to CSIC (EPSRC (EP/N021614/1) and Innovate UK (920035)) for funding and supporting this work and for facilitating the collaboration between the University of Naples Federico II and the University of Cambridge, which enabled Gianluigi Della Ragione to visit CSIC. They are also thankful to the Schofield Centre and its director, Professor Gopal Madabhushi, for their support with laboratory experiments. Fruitful advice and discussion with Professor Malcolm Bolton, Dr Sam Stanier and Professor Giulia Viggiani were also very valuable for the development of this project, together with the continuous help of Dr Geoff Eichhorn, Alessandro Fusco and Dr Cedric Kechavarzi in the laboratory.

NOTATION

B width of trapdoor
D_R relative density
H height of soil sample
I_R dilatancy index
i inflection point location
j Gaussian summation inflection point location
k factor relating horizontal and vertical displacements
p' mean stress level
r Gaussian summation inflection point location
S_{dip} strain representative of the drop associated with the dip in the Gaussian summation
S_h horizontal displacement
S_{max} maximum vertical settlement
S_{max}^{Surf} maximum surface settlement
S_{peak} strain representative of peak strain in the Gaussian summation
S_v vertical settlement
S_v^{Surf} surface settlement
w_D damage zone width
w_D^{Surf} damage zone width at soil surface
$\tilde{w}_D^{Surf}$ normalised damage zone width at soil surface
w_e trapdoor width estimate using distributed fibre optic sensing
x distance from centre of trapdoor
z height above the trapdoor
α shape factor to alter vertical location of inflection point
β shape factor to alter vertical location of inflection point
δ trapdoor displacement
$\tilde{\delta}$ normalised trapdoor displacement as a percentage
ε strain
η shape factor to alter vertical location of inflection point
ψ angle of dilation
Ω_D ultimate surface damage zone width overestimation ratio
Ω_t trapdoor width overestimation ratio

REFERENCES

Banks, V. J., Reeves, H. J., Ward, E. K., Raycraft, E. R., Gow, H. V., Morgan, D. J. R & Cameron, D. G. (2015). Media, sinkholes and the UK national karst database. In *Proceedings of the 14th multidisciplinary conference on sinkholes and the engineering and environmental impacts of karst (NCKRI symposium 5)* (eds D. H. Doctor, L. Land and J. B. Stephenson), pp. 223–230. Carlsbad, NM, USA: National Cave and Karst Research Institute.

Bolton, M. D. (1986). The strength and dilatancy of sands. *Géotechnique* **36**, No. 1, 65–78, https://doi.org/10.1680/geot.1986.36.1.65.

Chang, L. & Hanssen, R. F. (2014). Detection of cavity migration and sinkhole risk using radar interferometric time series. *Remote Sens. Environ.* **147**, 56–64.

Cooper, A. H. (2020). Geohazards caused by gypsum and anhydrite in the UK: including dissolution, subsidence, sinkholes and heave. *Geol. Soc., Lond., Engng Geol. Spec. Publs* **29**, No. 1, 403–423.

Cooper, A. H. & Calow, R. (1997). *Gypsum geohazards: their impact on development – project summary report*, Technical Report WC/97/17. Nottingham, UK: British Geological Survey.

Costa, Y. D., Zornberg, J. G., Bueno, B. S. & Costa, C. L. (2009). Failure mechanisms in sand over a deep active trapdoor. *J. Geotech. Geoenviron. Engng* **135**, No. 11, 1741–1753.

da Silva, T. S. (2017). *Centrifuge modelling of the behaviour of geosynthetic-reinforced soils above voids*. PhD thesis, University of Cambridge, Cambridge, UK.

da Silva Burke, T. S. & Elshafie, M. Z. (2021). Arching in granular soils: experimental observations of deformation mechanisms. *Géotechnique* **71**, No. 10, 866–878, https://doi.org/10.1680/jgeot.19.P.174.

Della Ragione, G. (2020). *Experimental and numerical study on the use of distributed fibre optic sensing technology as early warning system for sinkhole detection*. Master's thesis, University of Naples Federico II, Naples, Italy.

Dewoolkar, M. M., Santichaianant, K. & Ko, H. Y. (2007). Centrifuge modeling of granular soil response over active circular trapdoors. *Soils Found.* **47**, No. 5, 931–945.

Eichhorn, G. N. (2021). *Landslide–pipeline interaction in unsaturated silty slopes*. PhD thesis, University of Cambridge, Cambridge, UK.

Eichhorn, G. N., Bowman, A., Haigh, S. K. & Stanier, S. A. (2020). Low-cost digital image correlation and strain measurement for geotechnical applications. *Strain* **56**, No. 6, e12348, https://doi.org/10.1111/str.12348.

Guan, Z., Jiang, X. & Gao, M. (2013). A calibration test of karst collapse monitoring device by optical time domain reflectometry (BOTDR) technique. In *Proceedings of the 13th multidisciplinary conference on sinkholes and the engineering and environmental impacts of karst (NCKRI symposium 2)* (eds L. Land, D. H. Doctor and J. B. Stephenson), pp. 71–77. Carlsbad, NM, USA: National Cave and Karst Research Institute.

Guan, Z., Jiang, X. Z., Wu, Y. B. & Pang, Z. Y. (2015). Study on monitoring and early warning of karst collapse based on BOTDR technique. In *Proceedings of the 14th multidisciplinary conference on sinkholes and the engineering and environmental impacts of karst (NCKRI symposium 5)* (eds D. H. Doctor, L. Land and J. B. Stephenson), pp. 407–414. Carlsbad, NM, USA: National Cave and Karst Research Institute.

Guerrero, J., Gutiérrez, F., Bonachea, J. & Lucha, P. (2008). A sinkhole susceptibility zonation based on paleokarst analysis along a stretch of the Madrid–Barcelona high-speed railway built over gypsum- and salt-bearing evaporites (NE Spain). *Engng Geol.* **102**, No. 1–2, 62–73.

Gutierrez, F., Cooper, A. H. & Johnson, K. S. (2008). Identification, prediction, and mitigation of sinkhole hazards in evaporite karst areas. *Environ. Geol.* **53**, No. 5, 1007–1022.

Iglesia, G. R., Einstein, H. H. & Whitman, R. V. (2014). Investigation of soil arching with centrifuge tests. *J. Geotech. Geoenviron. Engng* **140**, No. 2, 04013005.

Igwe, O., Fukuoka, H. & Sassa, K. (2012). The effect of relative density and confining stress on shear properties of sands with varying grading. *Geotech. Geol. Engng* **30**, No. 5, 1207–1229.

Inaudi, D. (2017). Sensing solutions for assessing the stability of levees, sinkholes and landslides. In *Sensor technologies for civil infrastructures* (eds M. L. Wang, J. P. Lynch and H. Sohn), pp. 396–421. Cambridge, UK: Woodhead Publishing.

Jacobsz, S. W. (2016). Trapdoor experiments studying cavity propagation. In *Proceedings of the first Southern African geotechnical conference* (ed. S. W. Jacobsz), pp. 159–165. London, UK: Taylor & Francis Group.

Kechavarzi, C., Soga, K., de Battista, N., Pelecanos, L., Elshafie, M. Z. E. B. & Mair, R. J. (2016). *Distributed fibre optic strain sensing for monitoring civil infrastructure: a practical guide*. London, UK: ICE Publishing.

Klar, A., Dromy, I. & Linker, R. (2014). Monitoring tunnelling induced ground displacements using distributed fiber-optic sensing. *Tunn. Undergr. Space Technol.* **40**, 141–150.

Land, L. (2019). Sinkholes as transportation and infrastructure geohazards in southeastern new Mexico. In *Symposium on the application of geophysics to engineering and environmental problems 2019* (ed. D. Mills), pp. 145–150. Denver, CO, USA: Environmental & Engineering Geophysical Society.

Land, L., Cikoski, C. & Veni, G. (2018). Sinkholes as transportation and infrastructure geohazards in mixed evaporite-siliciclastic bedrock, southeastern new Mexico. In *Proceedings of the 15th multidisciplinary conference on sinkholes and the engineering and environmental impacts of karst (NCKRI symposium 7)* (eds I. D. Sasowsky, M. J. Byle and L. Land), pp. 357–367. Carlsbad, NM, USA: National Cave and Karst Research Institute.

Luna (Luna Innovations Incorporated) (2020). *Optical distributed sensor interrogator model ODiSI 6100: data sheet*. Blacksburg, VA, USA: Luna Innovations Incorporated.

Mair, R. J. (2008). Tunnelling and geotechnics: new horizons. *Géotechnique* **58**, No. 9, 695–736, https://doi.org/10.1680/geot.2008.58.9.695.

Marshall, A. M., Farrell, R. P., Klar, A. & Mair, R. (2012). Tunnels in sands: the effect of size, depth and volume loss on greenfield displacements. *Géotechnique* **62**, No. 5, 385–399, https://doi.org/10.1680/geot.10.P.047.

Möller, T. (2020). *Sinkhole formation: can a comparison with tunnelling illuminate the process?* Master's thesis, University of Cambridge, Cambridge, UK.

Rankin, W. J. (1988). Ground movements resulting from urban tunnelling: predictions and effects. In *Engineering geology of underground movements* (eds F. G. Bell, M. G. Colshaw, J. C. Cripps and M. A. Lovell), pp. 79–92. London, UK: Geological Society.

Sartain, N., Mian, J., O'Riordan, N. & Storry, R. (2011). Case study on the assessment of sinkhole risk for the development of infrastructure over karstic ground. In *Geotechnical safety and risk* (eds N. Vogt, B. Schuppener, D. Straub and G. Bräu), ISGSR 2011, pp. 635–642. Karlsruhe, Germany: Bundesanstalt für Wasserbau.

Son, M. & Cording, E. J. (2005). Estimation of building damage due to excavation-induced ground movements. *J. Geotech. Geoenviron. Engng* **131**, No. 2, 162–177.

Stanier, S. A., Blaber, J., Take, W. A. & White, D. J. (2015). Improved image-based deformation measurement for geotechnical applications. *Can. Geotech. J.* **53**, No. 5, 727–739.

Vorster, T. E., Klar, A., Soga, K. & Mair, R. J. (2005). Estimating the effects of tunnelling on existing pipelines. *J. Geotech. Geoenviron. Engng* **131**, No. 11, 1399–1410.

Zhang, C. C., Zhu, H. H. & Shi, B. (2016). Role of the interface between distributed fibre optic strain sensor and soil in ground deformation measurement. *Sci. Rep.* **6**, article 36469.

Zhao, Y., Gafar, K., Elshafie, M. Z. E. B., Deeks, A. D., Knappett, J. A. & Madabhushi, S. P. G. (2006). Calibration and use of a new automatic sand pourer. In *Physical modelling in geotechnics – 6th ICPMG '06* (eds C. W. W. Ng, Y. H. Wang and L. M. Zhang), pp. 265–270. London, UK: Taylor & Francis Group.